Determination of nitrogen spin concentration in diamond using double electron-electron resonance

Viktor Stepanov and Susumu Takahashi

Phys. Rev. B **94**, 024421 — Published 18 July 2016

DOI: 10.1103/PhysRevB.94.024421

Determination of nitrogen spin concentration in diamond using double electron-electron resonance

Viktor Stepanov

Department of Chemistry, University of Southern California, Los Angeles CA 90089, USA

Susumu Takahashi*

Department of Chemistry, University of Southern California, Los Angeles CA 90089, USA and

Department of Physics and Astronomy, University of Southern California, Los Angeles CA 90089, USA

Abstract

Diamond has been extensively investigated recently due to a wide range of potential applications of nitrogen-vacancy (NV) defect centers existing in a diamond lattice. The applications include magnetometry and quantum information technologies, and long decoherence time (T_2) of NV centers is critical for those applications. Although it has been known that T_2 highly depends on the concentration of paramagnetic impurities in diamond, precise measurement of the impurity concentration remains challenging. In the preset work, we show a method to determine a wide range of the nitrogen concentration (n) in diamond using a wide-band high-frequency electron spin resonance and double electron-electron resonance spectrometer. Moreover, we investigate T_2 of the nitrogen impurities and show the relationship between T_2 and n. The method developed here is applicable for various spin systems in solid and implementable in nanoscale magnetic resonance spectroscopy with NV centers to characterize the concentration of the paramagnetic spins within a microscopic volume.

PACS numbers: 76.30.-v, 76.30.Mi, 76.70.Dx, 81.05.uj

I. INTRODUCTION

A nitrogen-vacancy center (NV) in diamond is a promising candidate for investigation of spin physics[1,2] and applications to quantum information processing[3–5] and quantum nanoscale sensing[6–17] because of its remarkable properties including excellent photostability and capability to detect a single NV center at room temperature[1]. For the fundamental sciences and applications, long coherence of a NV center is critical. Coherence of a NV center highly depends on contents of paramagnetic impurities in diamond. In particular, nitrogen related impurities including well-known single substitutional nitrogen impurities (N spins, also known as P1 centers) are often abundant in many diamond crystals. For example, type-Ib and type-IIa diamonds typically contain nitrogen impurity concentration in the range of 10−100 parts-per-million (ppm) and tens of parts-per-billion (ppb), respectively. Coherence in such diamond crystals are largely affected by the concentration of nitrogen impurities[18,19].

Moreover, interest to fabricate ensembles of NV centers (NV concentration ∼1−100 ppm) have been rapidly growing for applications of NV-based quantum devices[20–22], showing that precise determination of the concentration of NV centers and N spins in diamond is highly useful. Unfortunately, currently available techniques have several limitations. For example, infrared absorption spectroscopy is a commonly-used technique to determine N spin concentration, however the sensitivity is often not high enough to measure type-IIa diamond[23]. Lineshape analysis of electron spin resonance (ESR) spectroscopy has been applied to determine the concentration of paramagnetic impurities. Although high precision of the spin concentration determination (~ 3 %) has been achieved at X-band ESR spectroscopy[24], the method remains challenging for wide applications as it highly depends on the choice of the reference sample[25], position of the samples in the cavity[26,27], spin relaxations[28] and requires precise knowledge of effect of samples on microwave fields[29,30], filling[25,30] and quality factors of the cavity[25,29], microwave and modulation field distributions over the sample volume[31–33].

In this article, we demonstrate a high-frequency (HF) double electron-electron resonance (DEER) technique to determine the concentration of paramagnetic impurities in solid-state systems with high precision and no reference sample. DEER spectroscopy is known to be a powerful technique to probe the magnetic dipole interaction between paramagnetic spins. For the investigation, we employ a home-built HF ESR/DEER spectrometer with capability to output in the frequency range of 107−120 GHz so that the system enables to

perform high spectral resolution ESR/DEER spectroscopy with different groups of spins. In the present demonstration, 115 GHz ESR/DEER spectroscopy is performed at room temperature. First, we measure HF ESR spectrum of paramagnetic spins in diamond which allows us to identify a type of impurities. The ESR spectrum analysis confirms that a majority of paramagnetic spins in both type-Ib and type-IIa diamonds are N spins. Then we perform pulsed ESR experiment to determine spin decoherence time (T_2) in the diamond crystals and DEER spectroscopy to determine the concentration of N spins in the range of 0.1−100 ppm. Finally, we investigate the relationship between the concentration of N spins and their spin decoherence time (T_2).

II. EXPERIMENT

For the investigation, we employed several synthetic diamond crystals including type-Ib and type-IIa crystals from DiAmante Industries, LLC[34], Element 6[35] and Sumitomo Electric[36]. The ESR/DEER measurements were performed using a home-built 115 GHz ESR/DEER spectrometer at room temperature. The 115 GHz ESR system employs a high-power (∼700 mW) solid-state source, quasioptical bridge, a corrugated waveguide and a 12.1 Tesla cryogenic-free superconducting magnet. The detection system is based on the induction mode detection to measure in-phase and quadrature components of ESR signals. The system also has a wide-band DEER capability (∼13 GHz) which is required for the present study. Details of the system have been described elsewhere[37,38].

A. Spin echo measurement

Figure 1 shows 115 GHz ESR measurements of type-Ib and type-IIa diamond crystals performed by monitoring the spin echo (SE) intensity as a function of magnetic fields. The type-Ib diamond crystal has a polished face normal to the [111] crystallographic axis while the type-IIa diamond crystal has a polished face normal to the [100] axis. In both measurements, the magnetic field was applied perpendicular to the polished surface. As shown in Fig. 1a, the ESR spectrum of the type-Ib diamond sample shows five pronounced peaks representing N spins ($\hat{H}_N = g\mu_B\vec{B}\hat{S} + \hat{S}\overleftrightarrow{A}\hat{I}$, $S = 1/2$, $g = 2.0024$, $I = 1$, $A_{x,y} = 82$ MHz, and $A_z = 114$ MHz). These five peaks originate (labeled as 1, 2, 3, 4, and 5) from the

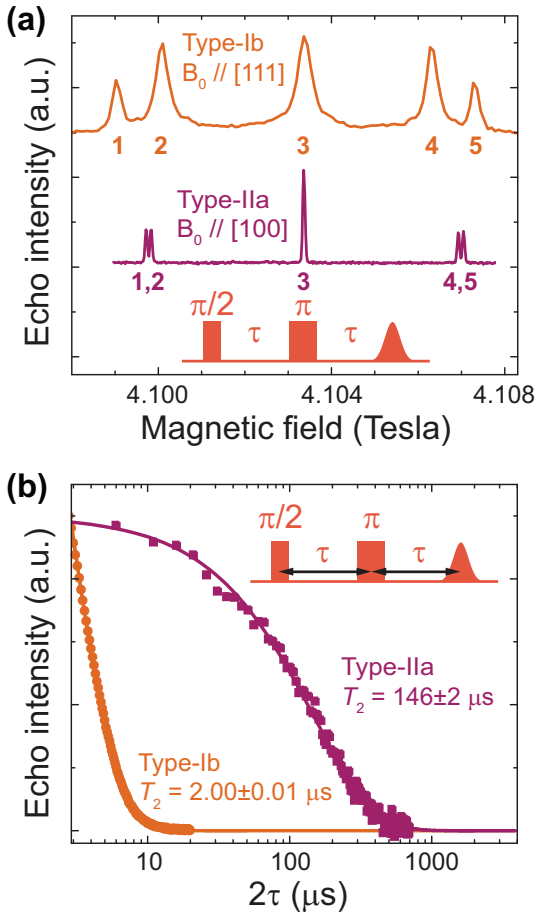

FIG. 1: Spin echo (SE) measurements of type-Ib and type-IIa diamond crystals. (a) SE intensity as a function of magnetic fields. The applied pulse sequence is shown in the inset. In the measurement of the type-Ib diamond, the durations of $\pi/2$ and π pulses were 150 ns and 250 ns and τ was 1.5 μs. The data were taken with 32 averages with 20 ms of the repetition time. In the measurement of the type-IIa diamond, the durations of the $\pi/2$ and π pulses were 250 ns and 450 ns and τ was 3 μs. The data were taken with 256 averages with 20 ms of the repetition time. The magnetic field was applied along the [111] direction for type-Ib crystals and the [100] direction for type-IIa. (b) SE intensity as a function of τ to measure spin decoherence time T_2. The decays of the SE were fitted by a single exponential function to extract T_2 (solid lines). The data of the type-Ib (type-IIa) diamond was taken with 128 (256) averages.

four principle axes of N spins, *i.e.*, [111], [11$\bar{1}$], [1$\bar{1}$1] and [$\bar{1}$11], and the hyperfine interaction to ^{14}N nuclear spin[39,40]. The intensity of the ESR signals represents the population of each group, with the population ratio corresponding to 1 : 3 : 4 : 3 : 1 for Group 1−5,

respectively. In addition, we measured the SE intensity of the N spins as a function of magnetic fields in the type-IIa diamond. As shown in Fig. 1a, the width of the observed signals were significantly narrower than those of the type-Ib crystal. Next, Fig. 1b shows spin decoherence time (T_2) measurements of the type-Ib and type-IIa samples. We observed that the SE decayed exponentially as a function of 2τ in both cases. As indicated in Fig. 1b, T_2 for the type-IIa diamond was nearly two orders of the magnitude longer than that of the type-Ib diamond while both samples have similar spin-lattice relaxation times (T_1) of several ms (data not shown). We also found that T_2 values of all groups were very similar.

B. Double electron-electron resonance spectroscopy

Next, we performed DEER spectroscopy to probe the magnetic dipole interaction between N spins. For DEER spectroscopy of the type-Ib diamond, the N spins at $B_0 = 4.099$ Tesla (Group 1), whose axis is along [111] and whose nuclear spin state is $|m_I = 1\rangle$, were used as probe spins (A spins). B spins (other N spins in Group 2−5 in Fig. 1a) were used as pump spins. Then we applied the three-pulse DEER sequence to probe the magnetic dipolar coupling between N spins in diamond[41]. As shown in the inset of Fig. 2a, the applied DEER sequence consisting of the SE sequence for A spins at the frequency of $\nu_A = 115$ GHz and a single π pulse for B spins at the frequency of ν_B. In the DEER spectroscopy, changes in the SE signal occur when the effective magnetic dipolar fields at A spins are altered by B spins that are flipped by the π pulse. As shown in Fig. 2b, four DEER signals of N spins were clearly observed as reductions of the SE intensity of A spins. The signals were centered at 114.971, 114.886, 114.801 and 114.772 GHz, corresponding to B spins in Group 2, 3, 4, and 5, respectively. Thus, the result confirms direct observation of the dipolar coupling between N spins in the type-Ib diamond. Similarly, we performed the DEER measurement with the type-IIa diamond, and, as shown in Fig. 2c, observed the DEER signals.

III. MODEL

A. Spin echo

There exist several processes which can contribute to the SE decay, including the spin flip-flops of N spin bath, the instantaneous diffusion, ^{13}C nuclear spins and the single spin

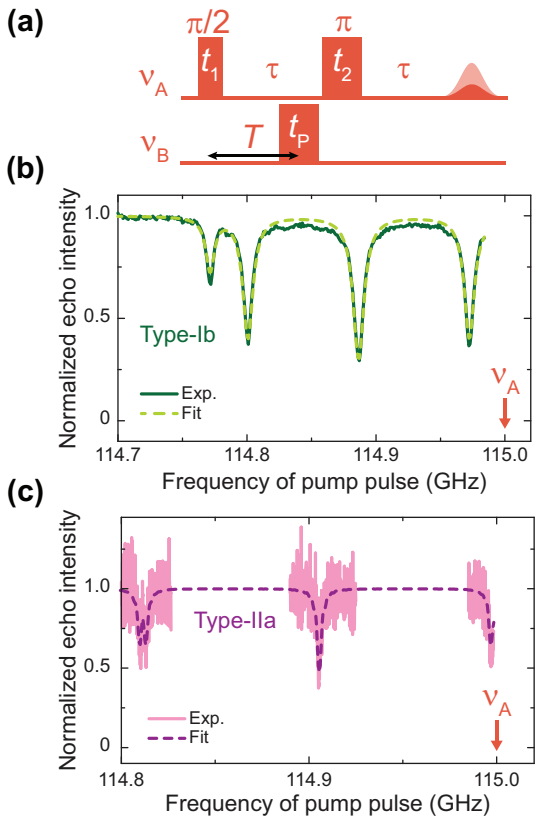

FIG. 2: Double electron-electron resonance (DEER) spectroscopy of the type-Ib and type-IIa diamond crystals. (a) three-pulse DEER sequence used in the experiment, where t_1 and t_2 denote duration of $\pi/2$ and π pulses for A spins, respectively. t_p is duration of π pulse for B spins. T is the delay of t_p from t_1. (b)&(c) DEER spectrum of N spins in type-Ib and type-IIa diamonds, respectively. The DEER signals were normalized by the SE signals. Experimental parameters were $t_1 = 250$ ns, $t_2 = 450$ ns, $t_p = 450$ ns, $\tau = 2.5$ μs, $T = 2$ μs in case of type-Ib diamond, and $t_1 = 250$ ns, $t_2 = 450$ ns, $t_p = 450$ ns, $\tau = 110$ μs, $T = 109.45$ μs in case of type-IIa diamond. The data of the type-Ib (type-IIa) diamond was taken with 128 (256) averages. Purple and brown dashed lines represent the best fit of experimental data using Eqn. 10.

flips (T_1 process). As reported previously, the spin flip-flop (also known as the spectral diffusion) is one of the major decoherence sources in type-Ib diamond crystals[18,40]. The spin flip-flop process causes dipolar-field fluctuations at the sites of the excited spins and the decoherence rate of this process linearly depends on the concentration of surrounding non-excited N spin bath[18,19]. On the other hand, in the case of type-IIa, it has been shown that the nuclear spin decoherence is pronounced[42,43]. In addition, the SE decay may be

speeded up by the process of instantaneous diffusion that manifests itself upon application of π pulse due to dipole-dipole interactions between the excited spins. In the case of the instantaneous diffusion process, the SE decay depends on the concentration of the excited spins, therefore the contribution of the instantaneous diffusion will be different between spin groups with different concentrations of N spins, *e.g.* group 1 and 3 in Fig. 1a. However our observation of similar T_2 times between different groups indicates that the instantaneous diffusion is insignificant in our experiments. The spectral diffusion due to T_1 process is also negligible in the present case because of the observed long T_1.

Next, we discuss the SE decay to estimate the spin flip-flop rate with the use of a model for the dipolar-coupled electron spins developed in Ref.[44]. According to Ref.[44], the SE decay due to the spectral diffusion is described by the following expression,

$$SE(2\tau) = \exp\left(-n\int_0^\infty f(W, W_{max})\int_V \left[1 - v_0(2\tau, W)\right] \mathrm{d}V\, \mathrm{d}W\right), \tag{1}$$

where W is the rate of the spin flip-flops of bath spins. v_0 represents SE signals of a single excited spin dipolar-coupled to a non-excited bath spin with the relative radius vector $(\vec{r}(r,\theta))$ given by,

$$v_0(2\tau, W) = \left[\left(\cosh R\tau + \frac{W}{R}\sinh R\tau\right)^2 + \frac{A^2}{4R^2}\sinh^2 R\tau\right]\exp\left(-2W\tau\right),$$

where $A \equiv \mu_0\mu_B^2 g_1 g_2(1-3\cos^2\theta)/(4\pi\hbar r^3)$ and $R^2 \equiv W^2 - \frac{1}{4}A^2$. μ_0 is the vacuum permeability, μ_B is the Bohr magneton, $\hbar$ is the reduced Planck constant, g_1 and g_2 are g-factors of the excited and bath spins, respectively. The integration over the sample volume V in Eqn. (1) takes into account all possible r and θ. The integration over W accounts for a distribution of the flip-flop rate within the sample where the distribution function $f(W, W_{max})$ is given by[44],

$$f(W, W_{max}) = \sqrt{\frac{3W_{max}}{2\pi W^3}}\exp\left(-\frac{3W_{max}}{2W}\right). \tag{2}$$

where $f(W, W_{max})$ is maximum at the flip-flop rate of $W = W_{max}$. Using the model above, we estimate an average flip-flop rate of N spins in diamond. We first consider a single exponential SE decay with $T_2 = 950$ ns ($\sim$the shortest T_2 observed in our experiments). We performed a fit using Eqn. (1) with a fixed N concentration to extract W_{max}. As shown in Fig. 3a, the SE model (Eqn. (1)) fits well with a single exponential decay with $T_2 = 950$ ns and the fit results give $\sim$4.9, $\sim$2.9, and $\sim$2 kHz of W_{max} for 60, 80 and 100 ppm of the

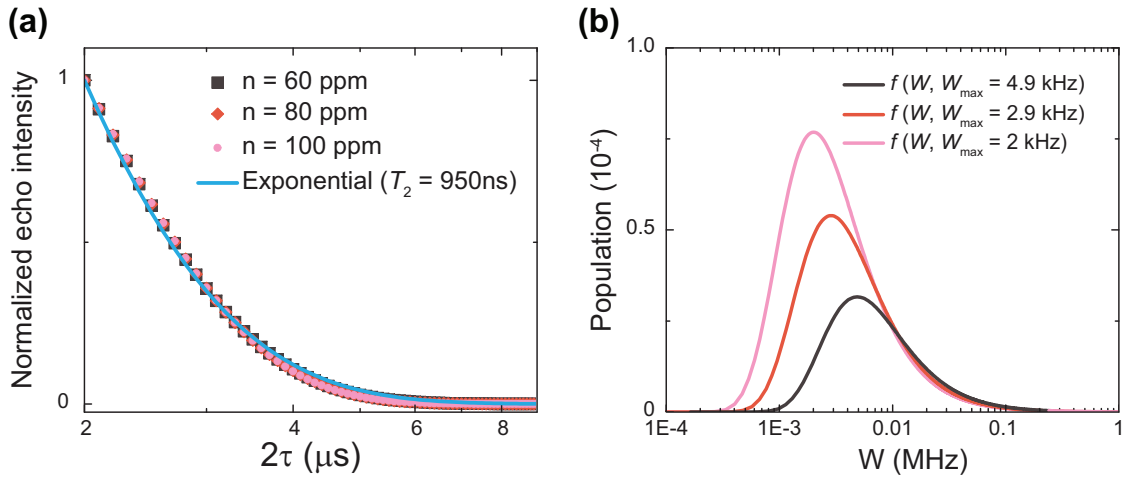

FIG. 3: (a) Analyses of a single exponential SE decay with $T_2 = 950$ ns (cyan) using Eqn. (1). 4.9, 2.9 and 2 kHz of W_{max} were obtained from the fits for 60 (black square), 80 (red diamond) and 100 (pink circle) ppm of N concentrations, respectively. (b) Flip-flop rate distribution among N spins obtained using Eqn. (2) for 4.9 (black), 2.9 (red) and 2 kHz (pink) of W_{max}.

concentrations, respectively. The flip-flop distribution function (Eqn. 2) for the obtained W_{max} are plotted in Fig. 3b. As shown in Fig. 3b, a major population of the flip-flop rate ranges from ∼1 kHz to ∼1 MHz. In addition, an average flip-flop rate is given by,

$$\langle W\rangle_{80\%} = \left[\sqrt{\frac{6W_{max}b}{\pi}}\exp\left(-\frac{3W_{max}}{2b}\right) - 3W_{max}\mathrm{erfc}\left(\sqrt{\frac{3W_{max}}{2b}}\right)\right]\Bigg|_{b=50W_{max}} \approx 7.1W_{max}$$

where the upper limit of the integration was set at 50 W_{max} (corresponding to 80% of the cumulative percentage) to avoid the divergence of the integral to evaluate the $\langle W\rangle$. Using values for $\langle W\rangle_{80\%}$, the average flip-flop events $2\tau\langle W\rangle_{80\%}$ during the DEER sequence (2τ = 3 μs for the sample with the shortest T_2) were estimated as 0.1, 0.06 and 0.04 for 60, 80 and 100 ppm, respectively. Moreover, for longer T_2 times, the flip-flop probability is expected to be even lower. With the given small flip-flop probability on the time scale of the DEER experiment, we consider the N spins to be in the static regime to model the DEER signal.

B. Double electron-electron resonance

In this section, we model DEER signals for ensemble N spins. The DEER signal is produced by probe N spins (A spins) interacting with resonant N spins to the pump pulse (B spins) and the rest of spins in diamond (C spins). C spins include both non-resonant

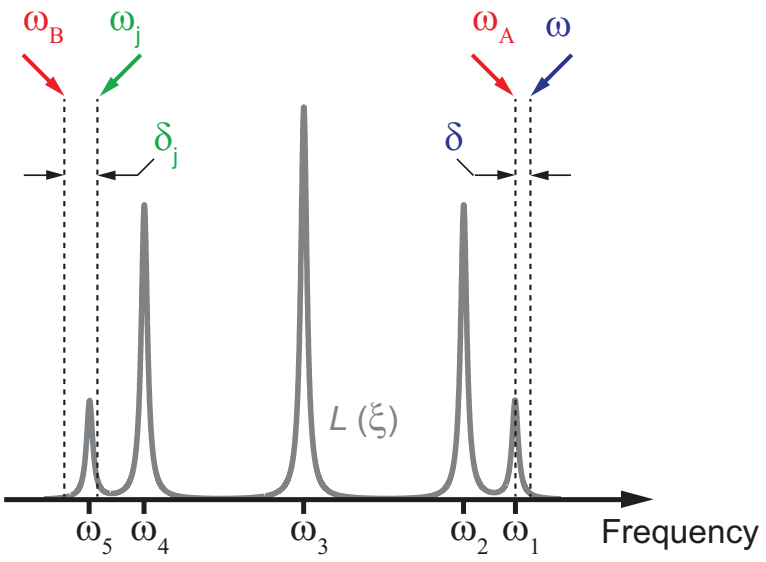

FIG. 4: Schematics for the DEER model. $L(\xi)$ is the lineshape function. ω_m is the center frequency of Group m (m=1−5). ω_A and ω_B are microwave frequencies of the probe and pump pulses, respectively. ω and ω_j are the Larmor frequencies of A and B spins, respectively. δ and δ_j are frequency offsets of A and B spins from the pump and probe frequencies, respectively. A and B spins were chosen close to the probe and pump frequencies, to indicate, that spins can be excited by a respective pulse with a small frequency offsets. However, in general, as in our consideration, they can be anywhere within the lineshape L.

N spins and nuclear spins. The center frequencies of ESR transitions of N spins are given by the Hamiltonian of N spins ($\hat{H}_N = g\mu_B \vec{B}\hat{S} + \hat{S}\overleftrightarrow{A}\hat{I}$). Moreover, all ESR transitions have equal linewidths due to randomly distributed N and nuclear spins in the diamond lattice, giving rise to inhomogeneously broadened spectral lines (*e.g.* Group 1−5 in Fig. 4). As shown previously[45,46], the inhomogeneous lineshape due to dipolar interactions between electron spins is expected to be Lorentzian while the lineshape due to electron-nuclear dipolar interactions is expected to be Gaussian. We here describe each spectral line by Lorentzian lineshape with a half-width of $\Delta\omega$ (the analysis of the type-IIa samples with the Gaussian lineshape was also tested (see Sect. IV-A)). Thus the total lineshape is given by $L(\xi) = \frac{1}{\pi}\sum_m f_m \frac{\Delta\omega}{\Delta\omega^2+(\xi-\omega_m)^2}$, where f_m and ω_m being fraction of spins and transition frequency of Group m, respectively.

Here, we focus on the case when magnetic field is applied along the [111] direction and a DEER lineshape is shown in Fig. 4. We start by considering a single A spin with the Larmor

frequency ω (see Fig. 4) as a two-level system (TLS) represented by Hamiltonian in units of frequency, $\hat{H}_0 = \omega\hat{S}_z$. During the application of the probe pulse with microwave frequency ω_A, applied at the center frequency of Group 1 (ω_1), the total Hamiltonian is given by $\hat{H} = \hat{H}_0 + \hat{H}_{MW} = \omega\hat{S}_z + 2\Omega\hat{S}_x \cos\omega_A t$, where $\Omega = g\mu_B b_1/\hbar$ and b_1 is the strength of the microwave field. The frequency offset (δ) in Fig. 4, defined as $\delta \equiv \omega - \omega_A$, is due to local magnetic fields from B and C spins, *i.e.* $\delta = g\mu_B(b_B + b_C)$, where $b_B(t) = \sum_j b_j(t)$ and $b_C(t) = \sum_k c_k(t)$, j and k are indexes of B and C spins, and $b_j(t)$ and $c_k(t)$ are magnetic fields produced by j-th B and k-th C spins at a single A spin, respectively. Due to the low probability of the flip-flop as discussed in Sec. III-A, δ is considered to be time-independent. Moreover, to calculate DEER signals below, we assume $|g\mu_b b_b/\hbar| \ll |\delta|$ for A spins contributing to SE signals in DEER experiment because of the low concentration ($< \sim 10^{19}$ spins/cm^3) and partial excitation of N spins. $|g\mu_b b_b/\hbar| \ll |\delta|$ is also commonly employed in dilute spin systems ($< 10^{20}$ spins/cm^3)[46]. The above assumptions ensure constant δ during DEER sequence.

First, we calculate SE signal produced by a single A spin during the pulse sequence $(t_1 - \tau - t_2 - \tau)$. The spin state by the end of the sequence ($|\psi_{2\tau}\rangle$) is given by,

$$|\psi_{2\tau}\rangle = \hat{U}_2(\tau)\hat{R}(t_2)\hat{U}_1(\tau)\hat{R}(t_1)\,|\psi_0\rangle\,, \tag{3}$$

where $|\psi_0\rangle$ is the initial state. $\hat{R}(t_i) \equiv \exp\left[-i\left(\delta\hat{S}_z + \Omega\hat{S}_x\right)t_i\right]$ is a propagator that describes evolution of TLS under the microwave excitation in the rotating frame with the microwave frequency (ω_A). In a matrix representation in the basis of $|+\rangle$ and $|-\rangle$ states, $\hat{R}(t_i)$ is given by,

$$\hat{R}(t_i) = \begin{pmatrix} c_i - i\frac{\delta}{\Omega_A}s_i & -i\frac{\Omega}{\Omega_A}s_i \\ -i\frac{\Omega}{\Omega_A}s_i & c_i + i\frac{\delta}{\Omega_A}s_i \end{pmatrix},$$

where $\Omega_A \equiv \sqrt{\delta^2 + \Omega^2}$, $c_i \equiv \cos\Omega_A t_i/2$ and $s_i \equiv \sin\Omega_A t_i/2$. U_i is a free evolution propagator defined as

$$\hat{U}_i(\tau) = \begin{pmatrix} e^{-i(\varphi_i+\phi_i)/2} & 0 \\ 0 & e^{i(\varphi_i+\phi_i)/2} \end{pmatrix},$$

with $\varphi_1 \equiv \frac{g\mu_B}{\hbar}\int_0^\tau b_B(t)\,\mathrm{d}t$, $\varphi_2 \equiv \frac{g\mu_B}{\hbar}\int_\tau^{2\tau} b_B(t)\,\mathrm{d}t$, $\phi_1 \equiv \frac{g\mu_B}{\hbar}\int_0^\tau b_C(t)\,\mathrm{d}t$ and $\phi_2 \equiv \frac{g\mu_B}{\hbar}\int_\tau^{2\tau} b_C(t)\,\mathrm{d}t$

Using Eqn. (3), the magnetic field component in the rotating frame along y-axis of a

single A spin with the initial state $|\psi_0\rangle = |-\rangle$, is calculated as

$$\begin{aligned}
\left\langle \hat{S}_y \right\rangle_s &= \langle \psi_{2\tau} | \, \hat{S}_y \, | \psi_{2\tau} \rangle \\
&= \left[\frac{\Omega}{\Omega_A} c_1 s_1 c_2^2 - \frac{\delta^2 \Omega}{\Omega_A^3} (c_1 s_1 s_2^2 + 2 s_1^2 c_2 s_2) \right] \cos 2\delta\tau \\
&+ \left[\frac{\delta^3 \Omega}{\Omega_A^4} s_1^2 c_2^2 - \frac{\delta \Omega}{\Omega_A^2} (2 c_1 s_1 c_2 s_2 + s_1^2 c_2^2) \right] \sin 2\delta\tau \\
&+ \frac{\Omega}{\Omega_A^3} c_2 s_2 \left[\delta^2 + \Omega^2 (c_1^2 - s_1^2) \right] \cos \delta\tau \\
&- \frac{\delta \Omega}{\Omega_A^4} s_2^2 \left[\delta^2 + \Omega^2 (c_1^2 - s_1^2) \right] \sin \delta\tau \\
&+ \left[-\frac{\Omega^3}{\Omega_A^3} c_1 s_1 s_2^2 \right] \cos (\varphi_1 - \varphi_2) + \left[\frac{\delta \Omega^3}{\Omega_A^4} s_1^2 s_2^2 \right] \sin (\varphi_1 - \varphi_2) .
\end{aligned}$$

After omitting the FID signals that are averaged out on the time scale of T_2^{*}[44], the $\left\langle \hat{S}_y \right\rangle_s$ is reduced to

$$\left\langle \hat{S}_y \right\rangle_s \approx \left[-\frac{\Omega^3}{\Omega_A^3} c_1 s_1 s_2^2 \right] \cos (\varphi_1 - \varphi_2) + \left[\frac{\delta \Omega^3}{\Omega_A^4} s_1^2 s_2^2 \right] \sin (\varphi_1 - \varphi_2) . \tag{4}$$

Similarly, $\left\langle \hat{S}_x \right\rangle_s$ in the rotating frame is found as

$$\left\langle \hat{S}_x \right\rangle_s \approx \left[-\frac{\Omega^3}{\Omega_A^3} c_1 s_1 s_2^2 \right] \sin (\varphi_1 - \varphi_2) + \left[-\frac{\delta \Omega^3}{\Omega_A^4} s_1^2 s_2^2 \right] \cos (\varphi_1 - \varphi_2) . \tag{5}$$

Next, the SE signal of a single A spin in the DEER measurement is calculated. When the pump pulse with the frequency (ω_B) excites B spins, the phase accumulated by the A spin during 2τ is expressed as

$$\delta\varphi \equiv \varphi_1 - \varphi_2 = \frac{g \mu_B}{\hbar} \sum_j \left(b_j (T - t_p/2) + \int_0^{t_p} b_j^{MW}(t) \, \mathrm{d}t + b_j^{MW}(t_p) \left[(\tau - T - t_p/2) - \tau \right] \right) , \tag{6}$$

where $b_j \equiv \mu_0 \mu_B g_B (3 \cos^2 \theta_j - 1) \sigma_j / (4\pi\hbar r_j^3)$ is a magnetic field produced by the j-th B spin at the A spin before the pump pulse is applied. σ_j is the spin state of the j-th B spin ($\sigma_j \pm 1/2$). $\vec{r}_j(r_j, \theta_j)$ is the radius vector of the dipole interaction between the j-th B spin and the A spin. $b_j^{MW} = b_j \left[\delta_j^2 + \Omega^2 (c_j^2 - s_j^2) \right] / \Omega_{B,j}^2$ with $\delta_j \equiv \omega_B - \omega_j$ (ω_j is the Larmor frequency of the j-th B spin. See Fig. 4), $\Omega_{B,j} \equiv \sqrt{\delta_j^2 + \Omega^2}$, $c_j \equiv \cos \Omega_{B,j} t/2$ and $s_j \equiv \sin \Omega_{B,j} t/2$. It is important to note that Eqn. (6) takes into account off-resonant excitation of the B spins which is represented by (σ_j, r_j, θ_j) and δ_j. Moreover, Eqn. (6) can be further simplified in

the present case ($t_p \ll 2\tau$ and $T \sim \tau$) to give

$$\delta\varphi \approx \frac{\mu_0}{4\pi}\frac{\mu_B^2 g_A g_B (2T)}{\hbar}\sum_j \frac{\Omega^2}{\delta_j^2+\Omega^2}\sin^2\left(\sqrt{\delta_j^2+\Omega^2}\frac{t_p}{2}\right)\frac{(3\cos^2\theta_j-1)\sigma_j}{r_j^3}.$$

Using the approach described in Ref.[38,45,46], the SE signal ($\langle\hat{S}_y\rangle_s$ and $\langle\hat{S}_x\rangle_s$) is averaged over B spins (r_j, θ_j, σ_j, δ_j),

$$\left\langle\langle\hat{S}_y\rangle_s\right\rangle_B \approx \left[-\frac{\Omega^3}{\Omega_A^3}c_1 s_1 s_2^2\right]\exp\left(-\frac{2\pi\mu_0\mu_B^2 g_A g_B T}{9\sqrt{3}\hbar}n\left\langle\sin^2\frac{\theta}{2}\right\rangle_L\right), \tag{7}$$

and

$$\left\langle\langle\hat{S}_x\rangle_s\right\rangle_B \approx \left[-\frac{\delta\Omega^3}{\Omega_A^4}s_1^2 s_2^2\right]\exp\left(-\frac{2\pi\mu_0\mu_B^2 g_A g_B T}{9\sqrt{3}\hbar}n\left\langle\sin^2\frac{\theta}{2}\right\rangle_L\right), \tag{8}$$

where $\langle\sin^2\frac{\theta}{2}\rangle_L \equiv \int_{-\infty}^{+\infty}\frac{\Omega^2}{(\xi-\omega_B)^2+\Omega^2}\sin^2\left(\sqrt{(\xi-\omega_B)^2+\Omega^2}\frac{t_p}{2}\right)L(\xi)\,\mathrm{d}\xi$.

To calculate DEER signal components in the rotating frame (I_x and I_y) produced by an ensemble of A spins, the DEER signals are first obtained for a single A spin with the $|\psi\rangle = |+\rangle$ initial spin state, similarly to above calculations, and averaged over $|+\rangle$ and $|-\rangle$ spin states with the use of thermal populations in each state, resulting in the thermal magnetization factor ($\Delta \equiv \tanh(\hbar\omega_A/2k_BT_0)$ where T_0 is sample temperature) for Eqns. (7) and (8). Next, the signals are averaged over the lineshape (L) to give

$$I_y = \Delta\left\langle -\frac{\Omega^3}{\Omega_A^3}c_1 s_1 s_2^2\right\rangle_L \exp\left(-\frac{2\pi\mu_0\mu_B^2 g_A g_B T}{9\sqrt{3}\hbar}n\left\langle\sin^2\frac{\theta}{2}\right\rangle_L\right),$$

and

$$I_x = \Delta\left\langle -\frac{\delta\Omega^3}{\Omega_A^4}s_1^2 s_2^2\right\rangle_L \exp\left(-\frac{2\pi\mu_0\mu_B^2 g_A g_B T}{9\sqrt{3}\hbar}n\left\langle\sin^2\frac{\theta}{2}\right\rangle_L\right).$$

where $\langle ...\rangle_L$ represents averaging over the inhomogeneous lineshape L. The latter being averaged out to zero when the probe frequency is centered with Group 1, thus the DEER intensity (I_Ω) is given by

$$\begin{aligned} I_\Omega &\equiv \sqrt{I_x^2+I_y^2} = |I_y| \\ &= \Delta\left\langle\frac{\Omega^3}{\Omega_A^3}c_1 s_1 s_2^2\right\rangle_L \exp\left(-\frac{2\pi\mu_0\mu_B^2 g_A g_B T}{9\sqrt{3}\hbar}n\left\langle\sin^2\frac{\theta}{2}\right\rangle_L\right)\exp\left(-\frac{2\tau}{T_2}\right), \end{aligned} \tag{9}$$

where the SE decay ($\exp(-2\tau/T_2)$) was added. In the case where the excitation bandwidth is larger that the inhomogeneous line ($\delta \ll \Omega$, then $\langle\sin^2\frac{\theta}{2}\rangle_L = 1$), Eqn. (9) reduces to the result obtained previously[38,41],

$$I_{DEER}(n) \sim \exp\left(-\frac{2\pi\mu_0\mu_B^2 g_A g_B T}{9\sqrt{3}\hbar}n\right).$$

Furthermore, the obtained $\langle \sin^2 \frac{\theta}{2} \rangle_L$ function in Eqn. (9) has been previously considered in the context of instantaneous diffusion[44,47] and DEER background signals in stabilized radical systems[48]. The SE intensity was also calculated previously without fully taking into account the off-resonant excitation[44,46]. In general, the off-resonant excitation not only reduces the tipping angle, but also results in the finite spin projection along the microwave field that was not considered in the previous models, however, in the present case, this contribution is critical.

In the present experiment, the microwave power is distributed across the sample, therefore Eqn. (9) has to be further averaged to account for distribution of Ω. Using the normalization signal ($N_\Omega = \Delta \langle \frac{\Omega^3}{\Omega_A^3} c_1 s_1 s_2^2 \rangle_L \exp(-2\tau/T_2)$), which is the SE signal with no pump pulse applied ($\langle \sin^2 \frac{\theta}{2} \rangle_L = 0$ in Eqn. (9)), the analytical expression of the DEER spectrum ($I_{DEER} = \langle I_\Omega \rangle_\Omega / \langle N_\Omega \rangle_\Omega$) is derived as,

$$\begin{aligned} &I_{DEER}\left(\omega_B, [\omega_A, t_1, t_2, t_p, T, \{f_m\}, \{\omega_m\}], [\Omega, \Delta\omega, n]\right) \\ &= \frac{1}{\langle \langle S_A \rangle_L \rangle_\Omega} \left\langle \langle S_A \rangle_L \exp\left(-\frac{2\pi \mu_0 \mu_B^2 g_A g_B T n}{9\sqrt{3}\hbar} \langle S_B \rangle_L \right) \right\rangle_\Omega , \end{aligned} \tag{10}$$

where

$$S_A = \frac{\Omega^3}{\Omega_A^3} \cos(\Omega_A t_1/2) \sin(\Omega_A t_1/2) \sin^2(\Omega_A t_2/2)$$

and

$$S_B = \frac{\Omega^2}{\Omega_B^2} \sin^2(\Omega_B t_p/2).$$

$1/\langle \langle S_A \rangle_L \rangle_\Omega$ is the normalization factor. $\langle ... \rangle_\Omega$ denote averaging over the distribution of the Rabi frequency Ω. Among the arguments, in the DEER measurement, ω_B is variable, and ω_A, t_1, t_2, t_p, T, $\{f_m\}$ and $\{\omega_m\}$ are fixed values. Fitting parameters (Ω, $\Delta\omega$ and n) are determined from analysis of the DEER spectrum as described in Sect. IV-A.

IV. DISCUSSION

A. Determination of N spin concentration

In this section, we present the analysis of DEER spectrum to obtain the concentration of N spins. The analysis was performed by fitting Eqn. (10) to the DEER signals. In the case

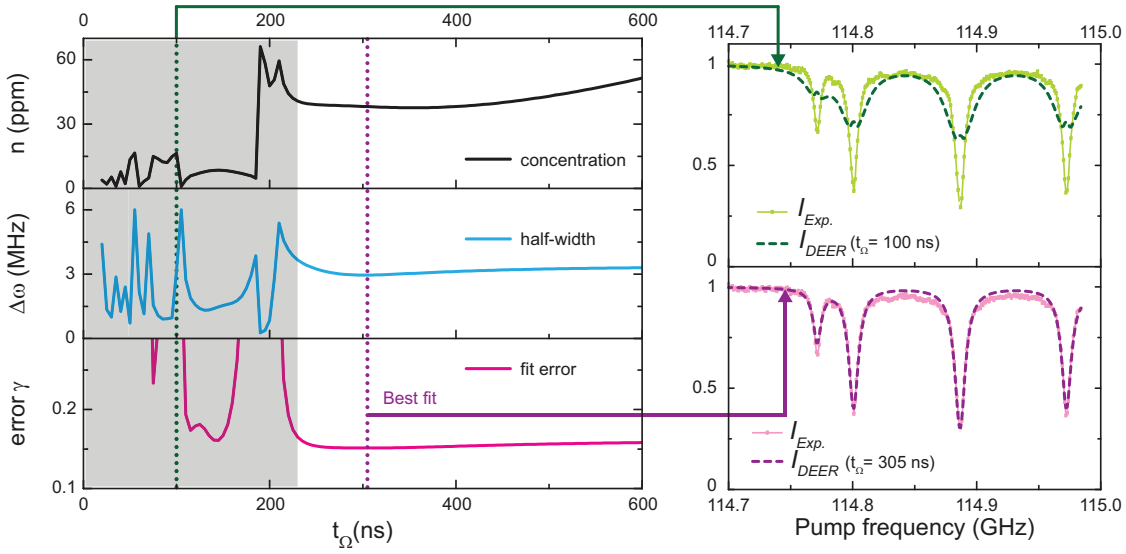

FIG. 5: Fit results of DEER spectrum. Left top, middle, bottom panels show concentration n of N spins, half-width $\Delta\omega$ of inhomogeneous lineshape and a fit error γ, respectively, as obtained from the fit at a fixed t_Ω values. The top (bottom) panel on the right shows the result of the fit obtained at $t_\Omega = 100$ ns (305 ns). The result with $t_\Omega = 305$ ns is the best fit. The grey shaded area on the left indicates fits with a large γ.

of the type-Ib diamond (Fig. 2b), the DEER pulse parameters ($t_1 = 250$ ns, $t_2 = 450$ ns, $t_p = 450$ ns, $T = 2$ μs, $\omega_A = 115$ GHz) and the experimentally obtained $\{\omega_m\}$ (114.7714, 114.8008, 114.8865 and 114.9724 GHz) were used. In addition, due to the magnetic field alignment along the [111] crystallographic direction, the fraction of spins in each spectral line $\{f_m\}$ was set to $\{1/12, 3/12, 4/12, 3/12, 1/12\}$. To account for the microwave field distribution, we used a sinusoidal function, $\Omega = \Omega_0(1 + \cos(2\pi x/\lambda_D))/2$, where x is a distance of N spin from the surface of the diamond, λ_D is the wavelength of the microwave in diamond ($\lambda_D = 1.08$ mm at 115 GHz) and Ω_0 is the maximum Rabi frequency in the diamond expressed in units of MHz, which was defined through the shortest duration of π pulse (t_Ω) in diamond as $\Omega_0 = 1/2t_\Omega$. Therefore, $\langle ... \rangle_\Omega$ in Eqn. (10) is equivalent to the averaging over the sample height h (the dimension of the diamond sample along the magnetic field and $h = 2$ mm in the present case).

With the parameters defined above, we performed the fit of the experimental DEER spectrum $I_{Exp}(\omega_B)$ using a least squares minimization procedure with a fixed value of t_Ω and fitting parameters of $\Delta\omega$ and n. The results of this procedure are shown in Fig. 5 where

TABLE I: Summary of $\Delta\omega$ and n for the studied type-IIa and type-Ib diamonds as extracted from the analyses of the DEER data. The errors of n and $\Delta\omega$ were estimated as 95 % confidence interval for the fit parameters.

n (ppm)	$\Delta\omega$ (MHz)	$t_\Omega\pm$ 5 (ns)
0.095±0.012	0.34±0.20	285
0.139±0.011	0.49±0.14	300
0.22±0.02	0.54±0.16	395
0.26±0.03	0.40±0.16	460
22.4±0.4	2.36±0.12	110
38.2±0.8	2.96±0.13	305
50.7±2.1	2.18±0.21	400
86.1±0.8	3.93±0.26	370

$\Delta\omega$, n and a fit error (γ) defined as a sum of squared residuals were plotted as a function of t_Ω (t_Ω = 20−600 ns). We performed the fit in the wide range of t_Ω with a step size of 5 ns. As seen in Fig. 5, the result of the fit highly depends on t_Ω and the fit error becomes smaller with $t_\Omega \gtrsim 220$ ns. The minimum error value was obtained at t_Ω of 305 ns. The values of $\Delta\omega$ and n for the best fit (dashed violet line in Fig. 5) were obtained as 2.96±0.13 MHz and 38.2±0.8 ppm, respectively, where the error was calculated as 95 % confidence interval for the fit parameter. Similarly, in the case of type-IIa diamond (Fig. 2b), the fit parameters were obtained as t_Ω = 300 ns, $\Delta\omega$ = 0.49±0.14 MHz and n = 0.14±0.01 ppm. The fit results for all studied diamonds are summarized in Table 1. The concentration for the shortest measured T_2 was found as 86.1±0.8 ppm, which is within the static model (Sec. III-A). In Fig. 6a, we present the concentration dependence of the inhomogeneous linewidth ($\Delta\omega$). $\Delta\omega$ at the high concentrations (10−100 ppm) depends strongly on the concentration of N spins, suggesting that the linewidth is governed by the dipolar coupling between N spins. In contrast, at the low concentrations (< 1 ppm), the linewidth is almost independent of the concentration, suggesting that the broadening is dominated by other impurities, most probably ^{13}C nuclear spins. We also analyzed the DEER spectra of the type-IIa diamond crystals with the Gaussian lineshape. We found that the fit results with

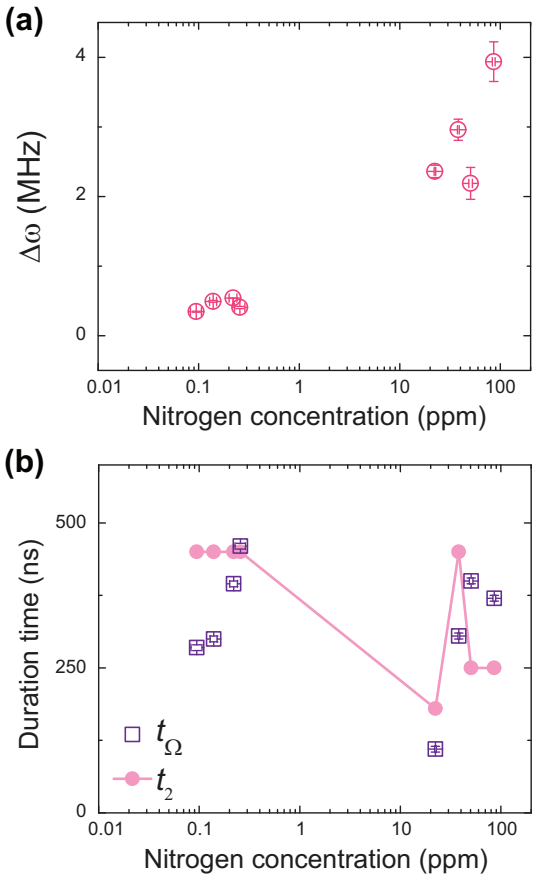

FIG. 6: (a) Summary of the obtained $\Delta\omega$. (b) Summary of the obtained t_Ω. t_2 is the duration of π-pulse used in the present study.

the Lorentzian lineshape are better and the discrepancy in the determined concentrations is within the error. On the other hand, the obtained t_Ω is independent of the concentration (n). t_Ω are also consistent with the experiment as shown in Fig. 6b, where the lengths of the microwave pulses were chosen to maximize the SE signals (the durations of the experimental π-pulse were 150-450 ns as shown in Fig. 6b). Possible reasons for the variations are different sizes of the diamond crystals and imperfect sample positioning[37].

B. T_2 of N spins vs N concentration

Finally, we discuss the relationship between T_2 and the concentration of N spins. As shown in Fig. 7, $1/T_2$ increases while the N concentration increases in both type-Ib and type-IIa diamond, however, the concentration dependence of the $1/T_2$ values are less pronounced in the type-IIa diamond. To analyze the observed concentration dependence of $1/T_2$, we

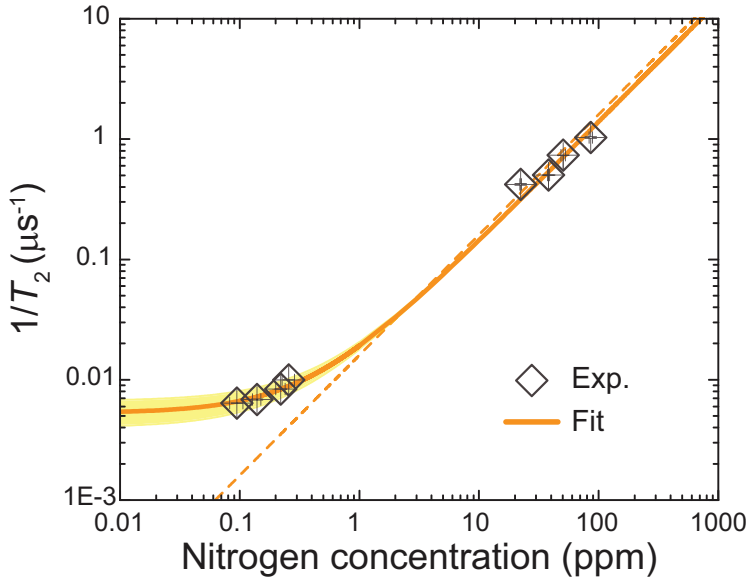

FIG. 7: $1/T_2$ of N spins as a function of the N concentration. Open squares represent experimentally obtained data, orange solid line is the best fit of the data to the model of decoherence rate described by Eqn. 11. Yellow region represents the plot of Eqn. 11 with the fixed Γ_C in the range of 150−250 μs and a slope C=0.0139 $\mu s^{-1}ppm^{-1}$ as obtained from the best fit of the data. Dashed orange line shows the best fit of the data using Eqn. 11 without the nuclear spin decoherence ($1/T_2^{^{13}C} = 0$).

considered the two decoherence processes including the spin flip-flop process of N spins ($1/T_2^N$), where the contribution from the N spin is considered to be proportional to the N concentration ($1/T_2^N \sim n$), and the ^{13}C decoherence ($1/T_2^{^{13}C}$). Thus, the decoherence rate (T_2) is considered by,

$$\frac{1}{T_2} = \frac{1}{T_2^N} + \frac{1}{T_2^{^{13}C}} = Cn + \frac{1}{T_2^{^{13}C}}, \tag{11}$$

where C is a proportional constant. As shown in Fig. 7, the data is well explained with Eqn. 11. From the fit using Eqn. 11, C was found to be 0.0139±0.0005 $\mu s^{-1}ppm^{-1}$ as well as $T_2^{^{13}C}$ to be 190±10 μs. The N spin concentration dependence in T_2 was observed in type-Ib and natural type-Ia diamond crystals although the previous study did not reveal the nuclear spin decoherence[18]. The obtained $T_2^{^{13}C}$ value is in a good agreement with the decoherence time due to ^{13}C nuclear spins[40,43].

V. SUMMARY

In summary, we demonstrated the capability of 115 GHz DEER spectroscopy at room temperature to determine a wide range of N spin concentrations. Using the pulsed 115 GHz ESR spectroscopy, we first determined T_2 in type-Ib and type-IIa diamond crystals and performed DEER spectroscopy to probe the magnetic dipole interaction between N spins. From the analyses of the SE decay and the DEER spectra, we determined concentrations of N spins in the range of $0.1 - 100$ ppm with no reference sample. Our DEER analysis to extract the spin concentration is strongly supported by the extracted N concentration dependence of the inhomogeneous linewidth and by the agreement of the estimated microwave power with our experimental values. Finally, we showed that the measurement of the N spin concentrations allows us to determine contributions of N spins and ^{13}C nuclear spins to T_2 quantitatively. The present method is applicable to determine the concentration of NV ensembles and various other spin systems in solid. In addition, by combining nanoscale magnetic resonance techniques based on NV centers, this method may pave the way to determine spin concentrations within a microscopic volumes.

VI. ACKNOWLEDGEMENT

This work was supported in part by the Searle Scholars Program, the USC Anton B. Burg Foundation and the National Science Foundation (DMR-1508661) (S.T.).

---

* Electronic address: susumu.takahashi@usc.edu

[1] A. Gruber, A. Dräbenstedt, C. Tietz, L. Fleury, J. Wrachtrup, and C. von Borczyskowski, Science **276**, 2012 (1997).

[2] F. Jelezko, I. Popa, A. Gruber, C. Tietz, J. Wrachtrup, A. Nizovtsev, and S. Kilin, Appl. Phys. Lett. **81**, 2160 (2002).

[3] F. Jelezko, T. Gaebel, I. Popa, M. Domhan, A. Gruber, and J. Wrachtrup, Phys. Rev. Lett. **93**, 130501 (2004).

[4] L. Jiang, J. S. Hodges, J. R. Maze, P. Maurer, J. M. Taylor, D. G. Cory, P. R. Hemmer, R. L. Walsworth, A. Yacoby, A. S. Zibrov, et al., Science **326**, 267 (2009).

[5] P. Neumann, R. Kolesov, B. Naydenov, J. Beck, F. Rempp, M. Steiner, V. Jacques, G. Balasubramanian, M. L. Markham, D. J. Twitchen, et al., Nat. Phys. **6**, 249 (2010).

[6] C. L. Degen, Appl. Phys. Lett. **92**, 243111 (2008).

[7] G. Balasubramanian, I. Y. Chan, R. Kolesov, M. Al-Hmoud, J. Tisler, C. Shin, C. Kim, A. Wojcik, P. R. Hemmer, A. Krueger, et al., Nature **455**, 648 (2008).

[8] J. R. Maze, P. L. Stanwix, J. S. Hodges, S. Hong, J. M. Taylor, P. Cappellaro, L. Jiang, M. V. G. Dutt, E. Togan, A. S. Zibrov, et al., Nature **455**, 644 (2008).

[9] J. M. Taylor, P. Cappellaro, L. Childress, L. Jiang, D. Budker, P. R. Hemmer, A. Yacoby, R. Walsworth, and M. D. Lukin, Nat. Phys. **4**, 810 (2008).

[10] S. Steinert, F. Ziem, L. T. Hall, A. Zappe, M. Schweikert, N. Götz, A. Aird, G. Balasubramanian, L. Hollenberg, and J. Wrachtrup, Nat. Commun. **4**, 1607 (2013).

[11] S. Kaufmann, D. A. Simpson, L. T. Hall, V. Perunicic, P. Senn, S. Steinert, L. P. McGuinness, B. C. Johnson, T. Ohshima, F. Caruso, et al., Proc. Natl. Acad. Sci. USA **110**, 10894 (2013).

[12] H. J. Mamin, M. Kim, M. H. Sherwood, C. T. Rettner, K. Ohno, D. D. Awschalom, and D. Rugar, Science **339**, 557 (2013).

[13] T. Staudacher, F. Shi, S. Pezzagna, J. Meijer, J. Du, C. A. Meriles, F. Reinhard, and J. Wrachtrup, Science **339**, 561 (2013).

[14] K. Ohashi, K. Ohashi, T. Rosskopf, H. Watanabe, M. Loretz, Y. Tao, R. Hauert, S. Tomizawa, T. Ishikawa, J. Ishi-Hayase, et al., Nano Lett. **13**, 4733 (2013).

[15] C. Müller, X. Kong, J.-M. Cai, K. Melentijević, A. Stacey, M. Markham, D. Twitchen, J. Isoya, S. Pezzagna, J. Meijer, et al., Nat. Commun. **5**, 4703 (2014).

[16] P. Maletinsky, S. Hong, M. S. Grinolds, B. Hausmann, M. D. Lukin, R. L. Walsworth, M. Loncar, and A. Yacoby, Nat. Nanotechnol. **7**, 320 (2012).

[17] C. Abeywardana, V. Stepanov, F. H. Cho, and S. Takahashi, SPIE Proc. **9269**, 92690K (2014).

[18] J. A. van Wyk, E. C. Reynhardt, G. L. High, and I. Kiflawi, J. Phys. D: Appl. Phys. **30**, 1790 (1997).

[19] Z.-H. Wang and S. Takahashi, Phys. Rev. B **87**, 115122 (2013).

[20] A. Jarmola, V. M. Acosta, K. Jensen, S. Chemerisov, and D. Budker, Phys. Rev. Lett. **108**, 197601 (2012).

[21] T. Wolf, P. Neumann, K. Nakamura, H. Sumiya, T. Ohshima, J. Isoya, and J. Wrachtrup, Phys. Rev. X **5**, 041001 (2015).

[22] C. Grezes, B. Julsgaard, Y. Kubo, W. L. Ma, M. Stern, A. Bienfait, K. Nakamura, J. Isoya, S. Onoda, T. Ohshima, et al., Phy. Rev. A **92**, 020301 (2015).

[23] K. Iakoubovskii, M. V. Baidakova, B. H. Wouters, A. Stesmans, G. J. Adriaenssens, A. Y. Vul', and P. J. Grobet, Dia. Rel. Mat. **9**, 861 (2000).

[24] V. Gancheva, N. D. Yordanov, F. Callens, G. Vanhaelewyn, J. Raffi, E. Bortolin, S. Onori, E. Malinen, E. Sagstuen, S. Fabisiak, et al., Radiat. Phys. Chem. **77**, 357 (2008).

[25] R. L. Blakley, D. D. Henry, W. T. Morgan, W. L. Clapp, C. J. Smith, and D. Barr, Appl. Spectros. **55**, 1375 (2001).

[26] N. D. Yordanov and M. Ivanova, Appl. Magn. Reson. **6**, 347 (1994).

[27] M. Mazur, Anal. Chim. Acta **561**, 1 (2006).

[28] S. S. Eaton and G. R. Eaton, Biol. Magn. Reson. **19**, 29 (2000).

[29] D. P. Dalal, S. S. Eaton, and G. R. Eaton, J. Magn. Reson. **44**, 415 (1981).

[30] V. Nagy, Appl. Magn. Reson. **6**, 259 (1994).

[31] N. D. Yordanov, B. Mladenova, and P. Petkov, Anal. Chim. Acta **453**, 155 (2002).

[32] N. D. Yordanov and B. Genova, Anal. Chim. Acta **353**, 99 (1997).

[33] D. Siebert, J. Dahlem, and V. Nagy, Anal. Chem. **66**, 2640 (1994).

[34] DiAmante Industries, LLC, http://www.di-amante.com/.

[35] Element 6, http://www.e6.com/.

[36] Sumitomo Electric USA, http://www.sumitomoelectricusa.com/.

[37] F. H. Cho, V. Stepanov, and S. Takahashi, Rev. Sci. Instrum. **85**, 075110 (2014).

[38] F. H. Cho, V. Stepanov, C. Abeywardana, and S. Takahashi, Methods Enzymol. **563**, 95 (2015).

[39] J. H. N. Loubser and J. A. Vanwyk, Rep. Prog. Phys. **41**, 1201 (1978).

[40] S. Takahashi, R. Hanson, J. van Tol, M. S. Sherwin, and D. D. Awschalom, Phys. Rev. Lett. **101**, 047601 (2008).

[41] A. D. Milov, K. M. Salikov, and M. D. Shirov, Sov. Phys. Solid State **23**, 565 (1981).

[42] L. Childress, M. V. G. Dutt, J. M. Taylor, A. S. Zibrov, F. Jelezko, J. Wrachtrup, P. R. Hemmer, and M. D. Lukin, Science **314**, 281 (2006).

[43] T. Gaebel, M. Domhan, I. Popa, C. Wittmann, P. Neumann, F. Jelezko, J. R. Rabeau, N. Stavrias, A. D. Greentree, S. Prawer, et al., Nat. Phys. **2**, 408 (2006).

[44] K. M. Salikhov, S. A. Dzuba, and A. M. Raitsimring, J. Magn. Reson. **42**, 255 (1981).

[45] W. B. Mims, Phys. Rev. **168**, 370 (1968).

[46] K. M. Salikhov, A. G. Semenov, and Y. D. Tsvetkov, Electron spin echo and its applications (Nauka Publishers, Novosibirsk, 1976).

[47] S. Agnello, R. Boscaino, M. Cannas, and F. M. Gelardi, Phys. Rev. B **64**, 174423 (2001).

[48] A. D. Milov, A. B. Ponomarev, and Y. D. Tsvetkov, Chem. Phys. Lett. **110**, 67 (1984).